IOP Publishing Superconductor Science and Technology
Supercond. Sci. Technol. 33 (2020) 044010 (13pp) https://doi.org/10.1088/1361-6668/ab6ee5

$YBa_2Cu_3O_{7-x}$ films with $Ba_2Y(Nb,Ta)O_6$ nanoinclusions for high-field applications

G Celentano[1,6], F Rizzo[1], A Augieri[1], A Mancini[1], V Pinto[1], A Rufoloni[1], A Vannozzi[1], J L MacManus-Driscoll[2], J Feighan[2], A Kursumovic[2], A Meledin[3,4,5], J Mayer[3,4] and G Van Tendeloo[5]

[1] ENEA Frascati Research Centre, Via E. Fermi 45, 00044 Frascati, Italy
[2] University of Cambridge, Dept. of Materials Science and Metallurgy, 27 Charles Babbage Rd., Cambridge, CB3 OFS, United Kingdom
[3] Central Facility for Electron Microscopy, RWTH Aachen University, 52074 Aachen, Germany
[4] Ernst Ruska-Centre for Microscopy and Spectroscopy with Electrons (ER-C), Forschungszentrum Jülich GmbH, 52428 Jülich, Germany
[5] Electron Microscopy for Materials Science (EMAT), Physics Department, Antwerp University, Antwerp, 2020, Belgium

E-mail: giuseppe.celentano@enea.it

Received 5 December 2019, revised 13 January 2020
Accepted for publication 22 January 2020
Published 20 February 2020

Abstract

The structural and transport properties of $YBa_2Cu_3O_{7-x}$ films grown by pulsed laser deposition with mixed 2.5 mol% Ba_2YTaO_6 (BYTO) and 2.5 mol% Ba_2YNbO_6 (BYNO) double-perovskite secondary phases are investigated in an extended film growth rate, $R = 0.02$–$1.8\ \mathrm{nm\ s^{-1}}$. The effect of R on the film microstructure analyzed by TEM techniques shows an evolution from sparse and straight to denser, thinner and splayed continuous columns, with mixed BYNO + BYTO (BYNTO) composition, as R increases from $0.02\ \mathrm{nm\ s^{-1}}$ to $1.2\ \mathrm{nm\ s^{-1}}$. This microstructure results in very efficient flux pinning at 77 K, leading to a remarkable improvement in the critical current density (J_c) behaviour, with the maximum pinning force density $F_p(\mathrm{Max}) = 13.5\ \mathrm{GN\ m^{-3}}$ and the irreversibility field in excess of 11 T. In this range, the magnetic field values at which the F_p is maximized varies from 1 T to 5 T, being related to the BYNTO columnar density. The film deposited when $R = 0.3\ \mathrm{nm\ s^{-1}}$ exhibits the best performances over the whole temperature and magnetic field ranges, achieving $F_p(\mathrm{Max}) = 900\ \mathrm{GN\ m^{-3}}$ at 10 K and 12 T. At higher rates, $R > 1.2\ \mathrm{nm\ s^{-1}}$, BYNTO columns show a meandering nature and are prone to form short nanorods. In addition, in the YBCO film matrix a more disordered structure with a high density of short stacking faults is observed. From the analysis of the $F_p(H, T)$ curves it emerges that in films deposited at the high R limit, the vortex pinning is no longer dominated by BYNTO columnar defects, but by a new mechanism showing the typical temperature scaling law. Even though this microstructure produces a limited improvement at 77 K, it exhibits a strong J_c improvement at lower temperature with $F_p = 700\ \mathrm{GN\ m^{-3}}$ at 10 K, 12 T and $900\ \mathrm{GN\ m^{-3}}$ at 4.2 K, 18 T.

Keywords: $Ba_2Y(Nb, Ta)O_6$ double perovskite, artificial pinning centers, pulsed laser ablation deposition, $YBa_2Cu_3O_{7-x}$ epitaxial films

(Some figures may appear in colour only in the online journal)

1. Introduction

The improvement in current-carrying capability through the controlled introduction of material defects able to pin magnetic flux vortices, i.e., artificial vortex pinning centers (APCs),

[6] Author to whom any correspondence should be addressed.

in superconducting $REBa_2Cu_3O_{7-x}$ (REBCO, RE = Y or rare earths) films has attracted great interest in the last two decades from both scientific and technological point of views. Several strategies have been successfully developed, mainly based on substrate surface modification, rare-earth substitution, the incorporation of nanolayers, and inclusions of nanoscale secondary phases, with remarkable improvement in the critical current density, J_c, properties of REBCO films [1–6]. Among them, one of the most studied and scalable methods is based on the incorporation of secondary phases segregated within the REBCO matrix during the film growth stage. This was first demonstrated on YBCO films by the pulsed laser deposition (PLD) technique by the addition of $BaZrO_3$ and, since then, replicated with many other Ba-based perovskites APCs and other film deposition techniques, such as metal–organic chemical vapour deposition (MOCVD) and chemical solution deposition with metal–organic salt precursors (CSD MOD) [3–10] (a comprehensive review can be found in [11]). In PLD nanocomposite films, secondary phases are typically incorporated as columnar or nanorod defects aligned along the YBCO *c* axis by a self-assembly process driven by strain minimization mechanisms [12]. This 1D-like feature has been extensively proven to be very effective for J_c improvements in the high temperature LN_2 (80–60 K) range. Nowadays, most of the REBCO coated conductor manufacturers have incorporated the APC technologies in their production lines so that REBCO conductors with optimized performances at high temperature and intermediate magnetic fields are available on the market [13]. More recently, the emerging interest in HTS materials for nuclear fusion and high energy physics high field applications motivated new research activities on REBCO in higher fields ($B > 13$–20 T) and lower temperature conditions ($T < 50$ K) [14–17]. However, at low temperature conditions REBCO has been poorly investigated so far and thus there is insufficient understanding of the most suitable defect landscape, neither of the required optimum pinning centres nor of the materials engineering needed to create them. Certainly, more in-depth studies are needed in order to fulfill the lack of knowledge in the low temperature–high field regime.

The first available data has shown that with the same approach of secondary phase additions, very remarkable improvements in J_c performance can be achieved at low temperature, down to 4.2 K [18–22]. It appears that a high density of secondary phases can produce very effective secondary effect pinning centres of a complex fine nature [12, 22]. At low temperatures, small sizes (with respect to the superconducting coherence length, for YBCO at $T = 0$ K, $\xi(0) \approx 0.3$ nm and 1 nm along the *c* axis or *ab* plane, respectively [12]), point-like, 0D defects are expected to play a major role in the vortex pinning contribution, and so the secondary effect pinning centres appear to produce this complex, very fine defect landscape. In fact, by an optimized MOCVD process, a very fine BZO column size (≈3.7 nm) with a dispersed Y_2O_3 nanoprecipitates landscape can be developed in heavily doped Zr (15 mol%) REBCO, achieving the record values of $J_c = 12$ MA cm^{-2} at 14 T or, equivalently, $F_p = 1.7$ TN m^{-3} [20]. Similar record performances ($F_p = 1.4$ TN m^{-3} at 17.5 T and 4.2 K) have been recorded for PLD SmBCO with 3.8 vol% $BaHfO_3$ addition by the low temperature growth (LTG) method which allows the development of a fan-shaped columnar system and a high density of low temperature effective random vortex pin points [19]. By the CSD method the successful incorporation of very small nanoparticles (5 nm) has led to a large improvement in low temperature performances due to the synergetic contribution of strain and core pinning by the nanoparticles themselves being their size, close to the coherence length [23]. A possible origin of low temperature effective pin points for vortices has been identified in local oxygen strain-induced nonstoichiometry, cation disorder or Cooper pair density depression localized at the YBCO/BZO nanorod interface [18, 24–27].

In this paper, the mixed 2.5 mol% Ba_2YTaO_6 (BYTO) and 2.5 mol% Ba_2YNbO_6 (BYNO) double perovskite secondary phases in $YBa_2Cu_3O_{7-x}$ films deposited by PLD are investigated by varying the film growth rate over two orders of magnitude, $R = [0.02$–$1.8]$ nm s^{-1}. It is reported in previous works that mixed BYTO + BYNO phases incorporated into the YBCO film matrix as dense and a fine columnar system exhibit very remarkable improvements in J_c behavior, not only at 77 K but also in lower temperatures down to 10 K [28–31]. By combining structural investigations by XRD, TEM analyses and J_c transport measurements carried out in wide temperature and magnetic field ranges, two effective microstructural landscapes have been identified. Slow deposition (low *R*) gives rise to a well-defined columnar system which is very effective in the high temperature range. This contrasts with the fast limit (high *R*) in which splayed nanorods, the meandering of columns and a high density of short stacking faults are promoted, resulting in more effective pinning at low temperatures. These two defect populations are developed in the optimal mix in the YBCO-BYNTO nanocomposite film deposited at $R = 0.3$ nm s^{-1}. This film exhibits very dense columns ($n_{col} \approx 2500$ μm^{-2}) corresponding to an equivalent magnetic flux density $B_{eq} = n_{col}$ $\Phi_0 \approx 5.2$ T. Also, the BYNTO columns have low diameters ($d_{BYNTO} = 5 \pm 1$ nm) leading to a remarkable performance over the whole temperature and magnetic field range. At 77 K, $F_p = 13.5$ GN m^{-3} and an irreversibility field in excess of 11 T, with maximum $F_p = 900$ GN m^{-3} at 10 K and 12 T. At higher rates, $R > 1.2$ nm s^{-1}, even though a limited improvement in J_c properties at 77 K are observed, a valuable J_c improvement at lower temperature with $F_p = 700$ GN m^{-3} at 10 K, 12 T and 900 GN m^{-3} at 4.2 K, 18 T is achieved. These results point the way to yet further improvements at low temperature and high magnetic field conditions, namely by further tuning and refining the YBCO nanocomposite growth conditions.

2. Experimental

YBCO-BYNTO composite films were deposited using a composite target with nominal 2.5 mol% Ba_2YTaO_6 (BYTO) and 2.5 mol% Ba_2YNbO_6 (BYNO) composition, by the pulsed laser ablation (PLD) technique using two excimer laser sources, XeCl and KF, emitting at wavelengths $\nu_L = 308$ and

248 nm, respectively. The dependence of the YBCO absorption coefficient upon the laser wavelength induces differences of about a factor of three in the growth rate per laser pulse at the given laser source ν_L values, being the smallest film growth at wavelength $\nu_L = 308$ nm [32]. The YBCO film growth rate has been further tuned by changing the laser repetition rate in the range $f_L = [1, 15]$ Hz. The film growth rates, R, have been calculated from the actual thickness of films measured by atomic force microscopy after patterning and/or by TEM cross sectional view. The calculated film growth rates span over two orders of magnitude from $R = 0.02\,\text{nm s}^{-1}$ to $1.8\,\text{nm s}^{-1}$. The nanocomposite target has been prepared by mixing and grinding the precursor oxides BaO, Y_2O_3, and Nb/Ta_2O_5 in stoichiometric quantities with pure YBCO powder and sintering in flowing oxygen at 950 °C. For all films, depositions occurred under the same conditions of temperature (840 °C), oxygen and pressure. The thickness of the films is in the range 150–230 nm. For only one film, the thickness has been increased to 900 nm. Films are deposited on a (00l) $SrTiO_3$ single crystal substrate. The deposition process and target preparation details can be found elsewhere [30, 33].

All samples have been analyzed by x-ray diffraction techniques with a Rigaku SmartLab diffractometer equipped with a 9 kW rotating anode and with a primary beam monochromator that grants CuKα1 radiation. The parallel beam geometry is used to record θ–2θ measurements and ω-scans across the (005)YBCO peak, and by using a Eulerian–Cradler polar figures and φ-scans have been acquired. Lattice parameters have been estimated by the Nelson–Riley extrapolation method assuming as uncertainty the error in the Nelson–Riley linear regression fit [34].

Critical current measurements were carried out on strips with defined geometry obtained after patterning with the usual optical photolithographic procedures. The strip widths used for this study are 30–50 μm. Critical current is defined with the electric field threshold $E_c = 1\ \mu\text{V cm}^{-1}$. J_c is simply obtained by dividing the critical current value by the cross sectional area of the strip. Pinning force is calculated as $F_p = J_c \times \mu_0 H$, while the irreversibility field values, H_{irr}, is the field above which the normalized pinning force density $F_p/F_p(\text{Max})$ is below 10^{-2}. For the angular dependence of the critical current density $J_c(\theta)$, the angle θ was defined as the angle between the magnetic field direction and the substrate normal direction, i.e., YBCO c axis. Samples are mounted into two cryostats equipped with 12 T and 18 T superconducting magnets. More details can be found in [33].

For TEM measurements, cross section and plan view lamellas were produced by focused ion beam (FIB, FEI Dual Beam Helios NanoLab). High- and low-angle annular dark field scanning transmission electron microscopy (HAADF STEM and LAADF STEM) imaging, STEM energy dispersive x-ray spectroscopy (STEM EDX) mappings were carried out on both on an FEI Titan probe Cs-corrected ChemiSTEM [33, 35] and QU-Ant-EM 'cubed' electron microscopes operated at 200 kV and 300 kV acceleration voltage respectively. Some of the STEM EDX mappings were carried out on a Tecnai Osiris TEM operated at 200 kV, equipped with a 'Super-X' EDX detector operated at 200 kV.

3. Results and discussion

3.1. Structural analyses

The effect of the growth rate R spanning over about two orders of magnitude from $R = 0.02$ to $1.8\,\text{nm s}^{-1}$ on the resulting film microstructure has been analyzed first.

As widely reported in previous works, BYNTO doping forms a dense and fine columnar system with the BYNTO phase segregated as columns aligned along the YBCO c axis [21, 28, 29]. In figures 1 and 2 the cross sectional view of samples deposited at the lowest ($R = 0.02\,\text{nm s}^{-1}$) and highest ($R = 1.8\,\text{nm s}^{-1}$) limits of the investigated film growth rate range are shown. At low values of R (figure 1(a)), well-defined and straight BYNTO columns are formed perfectly parallel to the film growth direction (corresponding to the YBCO c axis). Columns are grown from the STO substrate interface to the film surface across the entire film thickness. From the planar view investigation, the column diameter, d_{BYNTO}, and the density, n_{col}, have been accurately measured as $d_{BYNTO} = 12 \pm 2$ nm and $n_{col} = 540\ \mu\text{m}^{-2}$, corresponding to an equivalent magnetic flux density $B_{eq} = n_{col}\,\Phi_0 = 1.1$ T (Φ_0 is the magnetic flux quantum).

As often reported, BYNTO columns are decorated by few Y_2O_3 nanoparticles (about 20 nm in size, figure 1(a) right side and figure 1(b) yttrium EDX map) [29, 30]. Figure 1(b) shows STEM EDX mapping, revealing that distributions of Ta and Nb elements are uniformly distributed within the columns and confirming BYNTO columns composition. Figure 1(c) demonstrates simultaneously acquired high-resolution HAADF and LAADF STEM plan view images showing the cross section of a BYNTO column. The BYNTO column is well faceted with a semicoherent interface with YBCO. The occurrence of misfit dislocations at the BYNTO/YBCO interface can be very easily identified through geometric phase analysis (GPA) map analysis producing local peaks in the strain distribution (see figure 1(c), right image). The accumulation of strain is not revealed within the BYNTO column and YBCO matrix, indicating that these dislocations, generated at the interface to accommodate the lattice misfit, are an effective mechanism for the elastic strain release. On the other hand, the dark sharp contrast in the HAADF STEM image around the BYNTO nanocolumn (see figure 1(c), left image) is consistent with a lower YBCO oxygenation localized at the interface region. A strain-induced local oxygen nonstoichiometry has been invoked to explain the reduction of the c-axis strain of YBCO lattice close to the interface of YBCO/BZO nanocolumns [24, 36]. Although it provides an efficient strain relief mechanism, the oxygen deficiency in the YBCO layer surrounding the APC nanocolumns can lead to a local T_c depression. The overlap of nonstoichiometric YBCO layers, which easily results in samples with increasing doping levels, could be responsible for the observed progressive reduction in T_c typically observed in YBCO nanocomposite. A similar microstructure is recognized for samples deposited at increasing growth rates up to $R = 0.3\,\text{nm s}^{-1}$ [21], the main difference being related to the size and the density of the columns which get denser and finer as R increases. In

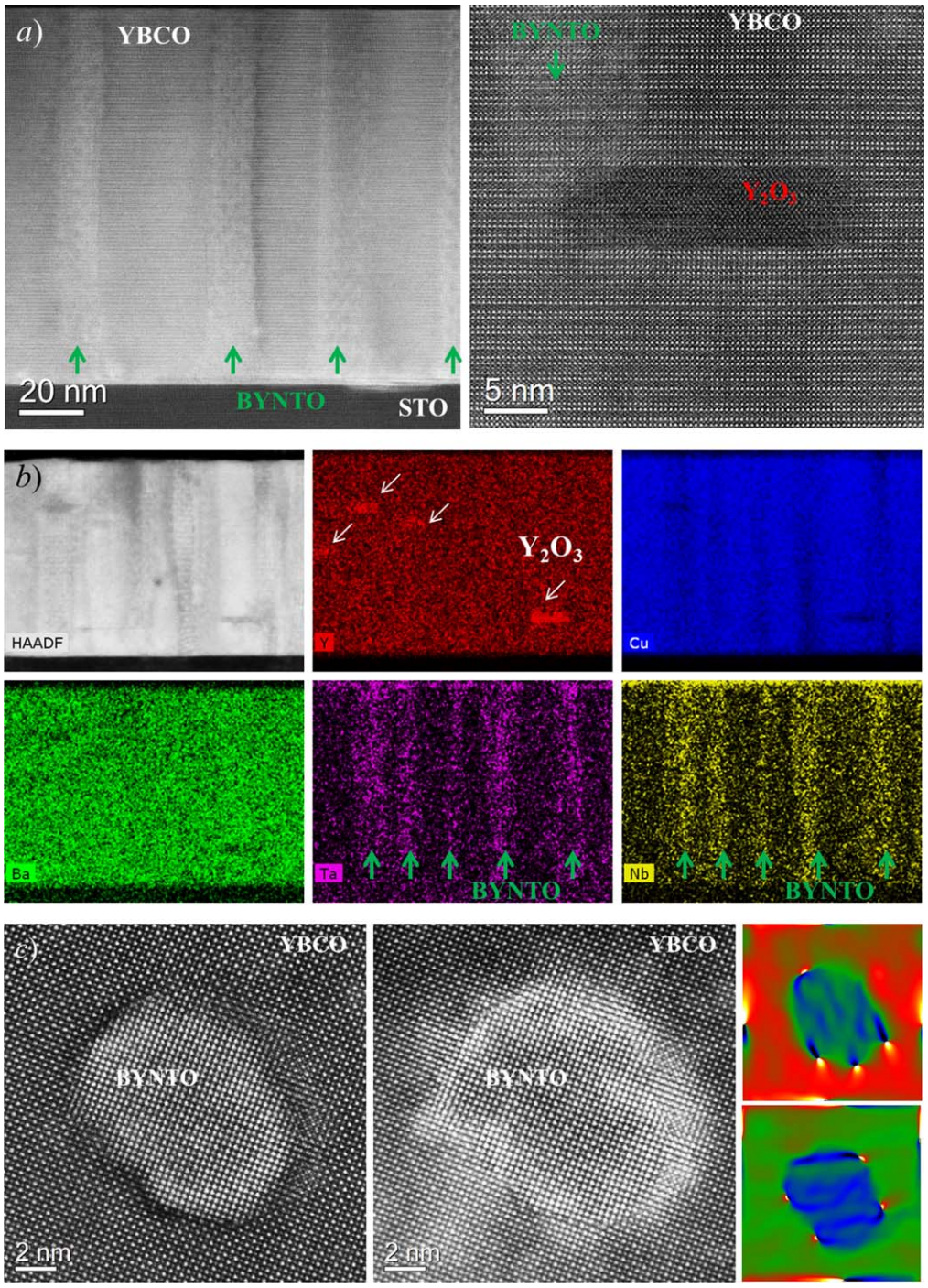

Figure 1. TEM investigations of YBCO-BYNTO films deposited at growth rate $R = 0.02\,\mathrm{nm\,s^{-1}}$. (a) Cross section view. *Left panel*: HAADF STEM overview of the film showing the BYNTO straight columns nucleated at the STO substrate and ending on the film surface (green arrows); *right panel*: high resolution HAADF STEM image showing BYNTO nanocolumn (marked by green arrow) decorated by Y_2O_3 nanoparticle. (b) Cross section view: HAADF STEM image showing the mapped area together with elemental Y, Ba, Cu, Ta and Nb EDX maps confirming BYNTO composition of the columnar structures and the Y_2O_3 composition of the decorating nanoparticles. (c) Plan view. *Left and central panels:* HAADF and LAADF STEM Z-contrast images. Dark sharp contrast in the HAADF STEM image and bright halos in the LAADF image around BYNTO nanocolumns correspond to the lower oxygenation on the interface and to the local strain, respectively. Interphase dislocations causing local strain can be visualized well by GPA maps (*right panel*).

addition, Y_2O_3 nanoparticle density shows an increasing trend with R, together with a reduction in size (from ≈20 nm to 5 nm in film deposited at $R = 0.3\,\mathrm{nm\,s^{-1}}$) even though no quantitative estimates have been carried out [30].

TEM investigations of the film deposited at $R = 1.8\,\mathrm{nm\,s^{-1}}$ reveal a different microstructure, as shown in figure 2. From the cross sectional view (figure 2(a)), the presence of splayed nanorods and meandered columns

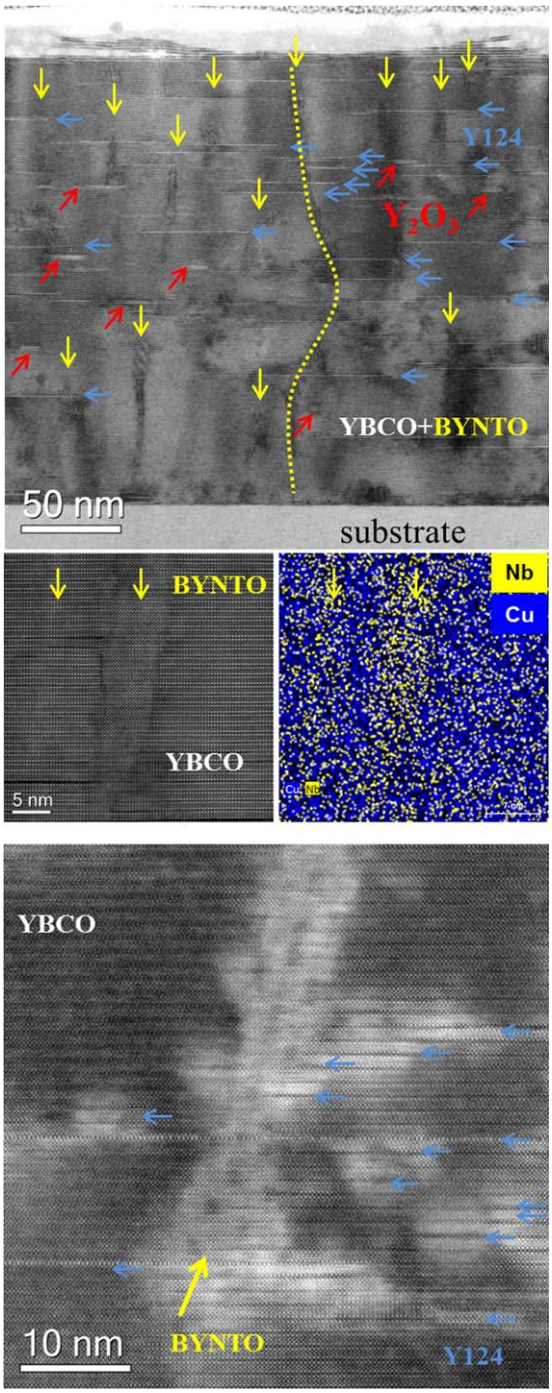

Figure 2. TEM investigations of YBCO-BYNTO films deposited at growth rate $R = 1.8$ nm s^{-1}. (a) *Top panel*: ABF STEM overview of the film showing BYNTO splayed nanorods (yellow arrows) and a BYNTO column meandering through the whole film thickenss (yellow dashed line). The presence of Y_2O_3 nanoparticles and stacking faults are identified by red and blue arrows, respectively; *bottom panel*: high resolution HAADF STEM image showing a BYNTO column in YBCO matrix and corresponding elemental Cu-Nb EDX map. (b) ADF STEM image showing the strain as brighter contrast features around the short Y124 intergrowths (blue arrows) and BYNTO nanocolumn. The chess plate-like contrast on BYNTO nanocolumn is produced by periodically spaced misfit dislocations with the brighter area corresponding to the dislocations strain and darker contrast to areas between the dislocations.

uniformly distributed within the YBCO matrix are observed together with a high density of stacking faults. The presence of yttria in the form of small segregated nanoparticles is confirmed. Nanorods are preferentially aligned to the YBCO *c*-axis and exhibit an average length of about 50 nm. In addition, BYNTO nanocolumns meandering from the substrate to the film surface (one example is highlighted by the yellow dotted path in figure 2(a)) can be recognized. Stacking faults consist of an extra Cu–O chain inserted between two Ba–O planes along the YBCO *c*-axis, resulting in a local variation of the stoichiometry ($Y_2Ba_4Cu_8O_{16}$, Y248 or Y124). This defect, created during the film growth stage in order to accommodate the strain along the *c*-axis, is promoted in extremely severe strain conditions, as in CSD YBCO with APC nanoparticles, or in pristine YBCO films close to the substrate interface region [37]. The presence of stacking faults has been reported often in previous works on YBCO with APC doping systems and BYNTO [28, 30, 38]. By comparing figures 1(a) and 2(a), an increase in the density of stacking faults with increasing R can be easily recognized. As can be seen in figure 2(a), stacking faults extend even more than 50 nm and most of them are induced by the BYNTO nanorods being generated from, or terminated at, the BYNTO interfaces. On the other hand, very short stacking faults can even be observed, as is clearly seen in figure 2(b). In that image, the diffraction contrast visualizes the strain in the sample as brighter contrast features localized around the short Y124 intergrowths and BYNTO nanocolumn. The chess plate-like contrast in the BYNTO nanocolumns corresponds to periodically spaced misfit dislocations. From the plan view images the BYNTO nanorod/column density has been estimated as $n_{col} \approx 1530\ \mu m^{-2}$, corresponding to $B_{eq} = 3.2$ T. The column diameter appears even smaller than the values reported for the other samples reaching a very remarkable size of $d_{BYNTO} = 3$ nm. However, some spread in the column diameter value has been observed with a d_{BYNTO} of up to 6 nm.

Figure 3 shows ABF and LAADF STEM cross sectional images on a thicker YBCO-BYNTO layer. This film has been deposited at the intermediate rate of $R = 1.2$ nm s^{-1}, increasing the film thickness up to about 900 nm in order to analyze the evolution of the defect landscape in thicker films. In figure 3(a), a cross-section overview of the sample is reported, from which the development of a very dense and columnar structure all over the film section can be recognized. Looking in more detail, it can be observed that this sample exhibits an intermediate character between lower and higher rate limits. In particular, there are bundles of columns that are partially interrupted at a certain film height (different from region to region) leaving some regions of the film cross section free of columnar structures. This feature can be in anticipation of the formation of nanorods instead of continuous columns observed for higher growing rates. The density of BYNTO columns remains rather constant across the film thickness. The presence of small yttria crystals

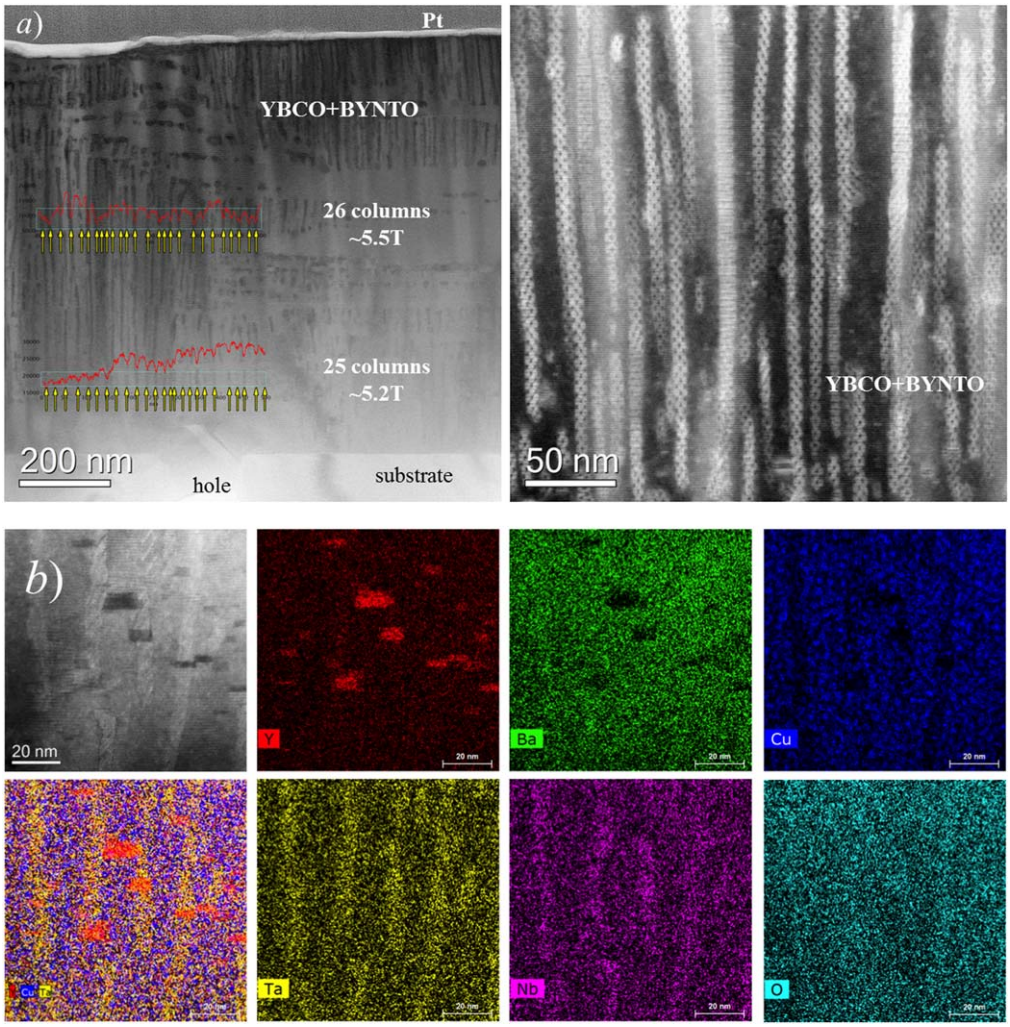

Figure 3. TEM investigations of YBCO-BYNTO films deposited at growth rate $R = 1.2$ nm s^{-1}. (a) *Left panel*: ABF STEM overview of the film showing the BYNTO columnar structures developed across the entire film thickness. Yellow arrows identify BYNTO columns in three different regions in which B has been estimated; *right panel*: LAADF STEM image showing the bright diffraction contrast around BYNTO columns. Some of the nanocolumns appear truncated. (b) HAADF STEM image together with corresponding elemental EDX maps for Y, Ba, Cu, O, Ta and Nb confirm BYNTO nanocolumns and Y_2O_3 composition.

Table 1. Summary of structural parameters on YBCO-BYNTO obtained by TEM and XRD investigations: d_{BYNTO} = BYNTO average column diameter, n_{col} = BYNTO column density, $B_{eq} = n_{col}\,\Phi_0$ is the equivalent magnetic flux density. All values are calculated by plan view images unless marked by (*). Samples deposited by XeCl laser source are highlighted in gray.

Laser repetition rate (Hz)	Film growth rate (nm s^{-1}) ± 10%	d_{BYNTO} (nm)	n_{col} (μm^{-2}) B_{eq}^{-1} (T)	T_c (K)	c_{YBCO} (nm) ± 0.001 nm	FWHM (005) YBCO ω-scan
1	0.02	12 ± 2	540/1.1	89.3	1.169	0.12°
5	0.1	8 ± 1	960/2	89.9	1.17	0.12°
10	0.3	5 (*)	2500/5.2 (*)	89.2	1.169	0.13°
10	1.2	5 (*)	—/5.5 (*)	88.7	—	—
10	1.4	—	—	88.6	1.171	0.14°
15	1.8	3–6	1530/3.2	87.2	1.170	0.24°

decorating BYNTO columns or nanorods is still observed, as confirmed by the EDX map shown in figure 3(b).

From the TEM investigations it is determined that the d_{BYNTO} size varies from about 12 nm, down to about 3 nm (see table 1). As already reported in our previous work, d_{BYNTO} is affected by f_L [21] independent of the laser wavelength adopted for the film growth. This behaviour indicates that, under the present investigated growth conditions, the column size is mainly determined by the surface diffusion time $t \propto 1/f_L$. Adatoms within the spatial range $\sqrt{(D_S t)} \approx \sqrt{(D_S/f_L)}$, with D_S being the diffusion coefficient of BYNTO elements at the YBCO surface, will be able to

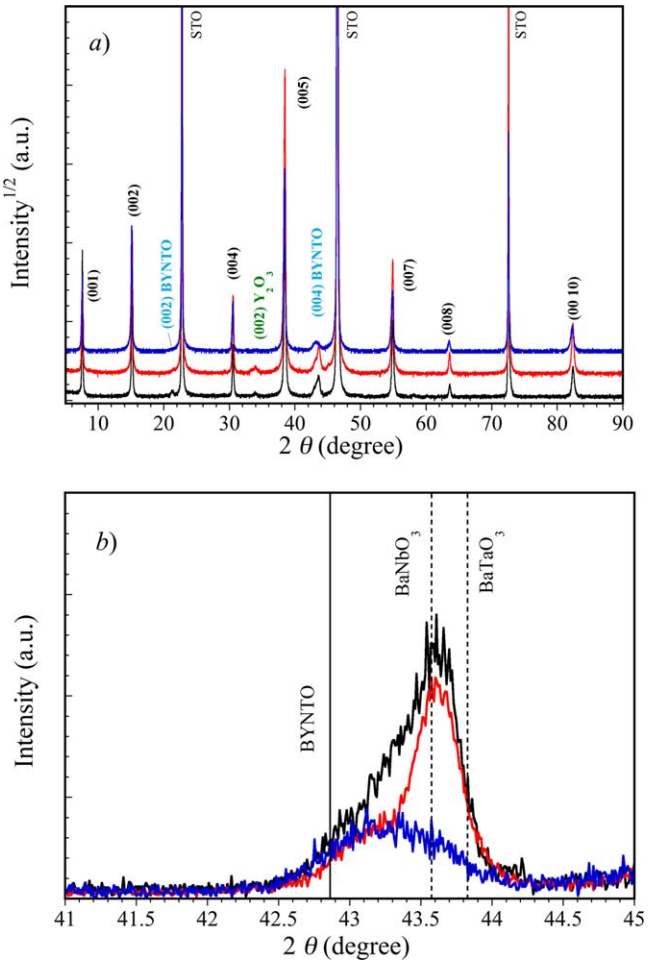

Figure 4. (a) X-ray θ-2θ diffraction patterns recorded for YBCO-BYNTO films deposited at different growth rates: $R = 0.02$ nm s^{-1} (black line), 0.3 nm s^{-1} (red line) and 1.8 nm s^{-1} (blue line). (b) Detail of the (004) BYNTO peak. The continuous line marks the BYNTO bulk peak position whereas dashed lines mark the $BaNbO_3$ and $BaTaO_3$ (002) peaks.

migrate to the growing BYNTO nuclei before the new incoming materials arrive on the film surface. From that time on, the nuclei lateral growth will proceed only through bulk diffusion process, which is orders of magnitude slower than surface diffusion [12], thus BYNTO preferential growth along the *c*-axis will result. The dependence of d_{BYNTO} upon the deposition temperature, T_g, has often been reported for $BaZrO_3$ and $BaHfO_3$ APC systems [39, 40]. In those cases, an increase in column size was reported with T_g, which is consistent with the accelerated surface diffusivity of the elements due to increase in the diffusion coefficient D_S with temperature. Moreover, it can be observed that the column or rod diameters exhibit a similar value and same range of variability (≈5–≈15 nm), indicating that this might be a general property of the Ba-based perovskite APC systems.

In figure 4(a), the XRD θ–2θ spectra recorded on films deposited at different growth rates are shown. As can be seen, all spectra reveal good *c*-axis oriented YBCO growth as determined by the presence of sharp YBCO (00*l*) peaks and without any traces of peaks related to other YBCO grain orientations. The presence of a minor peak centered at 34° suggests that the formation and segregation of crystallites of Y_2O_3 occurred during the growth. The presence of a minor fraction of yttria inclusions in YBCO films is not surprising, being widely reported in high quality YBCO films [41]. The calculated *c*-axis lattice parameters do not reveal any clear dependence with *R*, whose values range between 1.169 nm to 1.171 nm (±0.001 nm) (see table 1), similar to the values measured for pristine YBCO epitaxial films on STO substrates deposited in the same film growth rate range.

BYNTO particles grow cube-on-cube with respect to the YBCO lattice as recognized by the presence of only the (002) and (004) peaks in the θ–2θ patterns. However, the (004) BYNTO peaks exhibit a broad and smeared structure, as is more clearly discernible in figure 4(b). This structure clearly depends on the growth rate: at low *R*, an asymmetric peak at about 43.6° can be recognized with a broad low angle tail. The peak weakens with increasing *R*, eventually disappearing or being incorporated into a broader band centered at about 43.2°. Interestingly, (004) BYNTO is shifted to higher angles with respect to the bulk values (about 42.86°, continuous line in figure 4(b)) of either BYNO or BYTO phases. Similar features were observed in a previous study on mixed niobate/cuprate $Ba_4Y_2CuNbO_y$ secondary phase additions into YBCO films. In that case, the shift and the broadening of the peaks in the XRD pattern were attributed to the formation of Ba_2YNbO_6 with variable yttrium content [42]. By analogy, in the present work, the formation of $Ba_2Y_x(Nb,Ta)_{2-x}O_6$ ($0 \leqslant x \leqslant 1$) can be assumed, with some loss of yttrium in the phase being responsible for the observed peak shift and the broadening feature due to the inhomogeneous distribution of the yttrium content in the BYNTO segregated particles. In this framework, the increasing Y loss induces a shift in the peak towards higher angle values. In figure 4(b), the positions of (002) peaks for $BaNbO_3$ and $BaTaO_3$ are also marked by dashed-dotted lines as reference for $x = 0$ limits [43]. As can be seen, the peaks in the case of films deposited at $R = 0.02$ and 0.1 nm s^{-1} are comprised within these limits, with the low angle side of the (004) reflections smeared over the whole angular range up to the BYNTO bulk value ($x = 1$), suggesting that an inhomogeneous distribution of Y into BYNTO particles incorporated within the YBCO matrix has been achieved during the film growth spanning the full $0 \leqslant x \leqslant 1$ range. From these features, at low *R*, considerable Y loss in BYNTO is derived, $x \approx 0$ being the largest components. The increase in *R* hinders the tendency of the loss in yttrium, as suggested by the shift of the band peak to lower angles approaching the $x \approx 1$ limit. The loss of Y can be justified on the basis of reduction of strain at the BYNTO/YBCO interface. The lattice misfit between YBCO and BYNTO along the *c*-axis can be calculated as $(3 \times c_{BYNTO} - 2 \times c_{YBCO})/(2 \times c_{YBCO}) = -0.083$, whereas the misfit with respect to $BaNbO_3$ (or $BaTaO_3$) is ≈−0.065 (calculated as $(3 \times c_{BYN(T)O} - c_{YBCO})/c_{YBCO}$), thus a great benefit in terms of the reduction of interfacial strain would be derived by the Y release from BYNTO lattice. The resulting excess of Y likely causes dense Y_2O_3 nanocrystals to form, decorating the BYNTO columns in the samples.

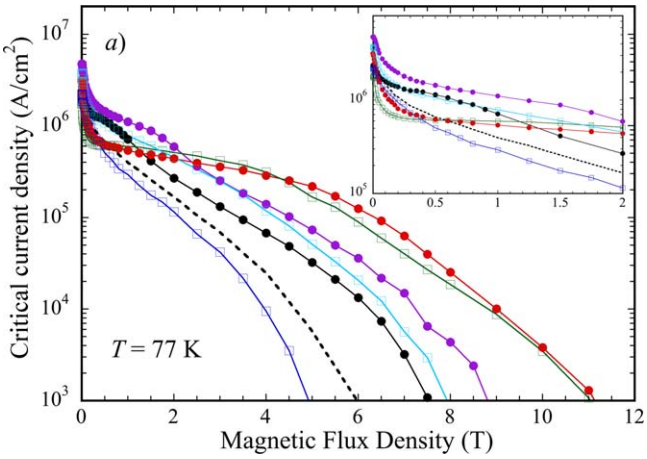

Figure 5. $J_c(B)$ curves collected at 77 K for samples deposited with growth rates $R = 0.02\,\mathrm{nm\,s^{-1}}$ (black circles), 0.1 (purple circles), 0.3 (red circles), 1.2 (green squares), 1.4 (light blue squares), and $1.8\,\mathrm{nm\,s^{-1}}$ (blue squares). In the insert, details of the low field region are emphasized. A pristine YBCO sample curve is also reported for comparison (dashed line).

3.2. YBCO dc transport properties

In figure 5 the $J_c(H)$ curves measured at 77 K for YBCO-BYNTO samples deposited at different growth rates are shown. As can be seen, the growth rate mainly affects the in-field behaviour, rather than J_c self-field values. All samples show improved performances with respect to pristine YBCO film. Only the sample deposited at $R = 1.8\,\mathrm{nm\,s^{-1}}$ (the upper limit of the investigated range) does not exhibit any valuable increase over the whole magnetic field range. In the low growth rate range ($R \leqslant 0.3\,\mathrm{nm\,s^{-1}}$), $J_c(H)$ curves show a better in-field behavior in the low field region with the occurrence of a marked plateau whose extension increases with the growth rate from ~0.5 T to ~4 T for $R = 0.02\,\mathrm{nm\,s^{-1}}$ and $0.3\,\mathrm{nm\,s^{-1}}$, respectively. The irreversibility field $\mu_0 H_{irr}$ largely increases, reaching, for the sample at $R = 0.3\,\mathrm{nm\,s^{-1}}$, the record value of ~11 T. As already pointed out, the J_c plateau can be related to the occurrence of the matching field effect, the result of a cooperative action of the columnar system characterized by the very favourable and pinning-effective condition in which each vortex line is individually pinned by a single BYNTO column. This effect, whose extension is proportional to the column density, has already been observed in BYNTO films [29, 30]. Interestingly, the thicker sample grown at $R = 1.2\,\mathrm{nm\,s^{-1}}$ exhibits very similar magnetic field dependence if compared to the sample grown at $R = 0.3\,\mathrm{nm\,s^{-1}}$, consistent with the similar BYNTO column density revealed by TEM. This trend is confirmed for increasing growth rates ($R = 1.4$ and $1.8\,\mathrm{nm\,s^{-1}}$), where the low field plateau progressively disappears and the J_c in-field behaviours weaken, becoming similar to pristine YBCO for $R = 1.8\,\mathrm{nm\,s^{-1}}$. As observed by TEM investigations, for these high rate values, BYNTO is preferably assembled as a short splayed nanorods system, and this likely reduces the effective contribution to vortex pinning provided by columnar systems when $\mu_0 H$ is parallel to the YBCO *c* axis.

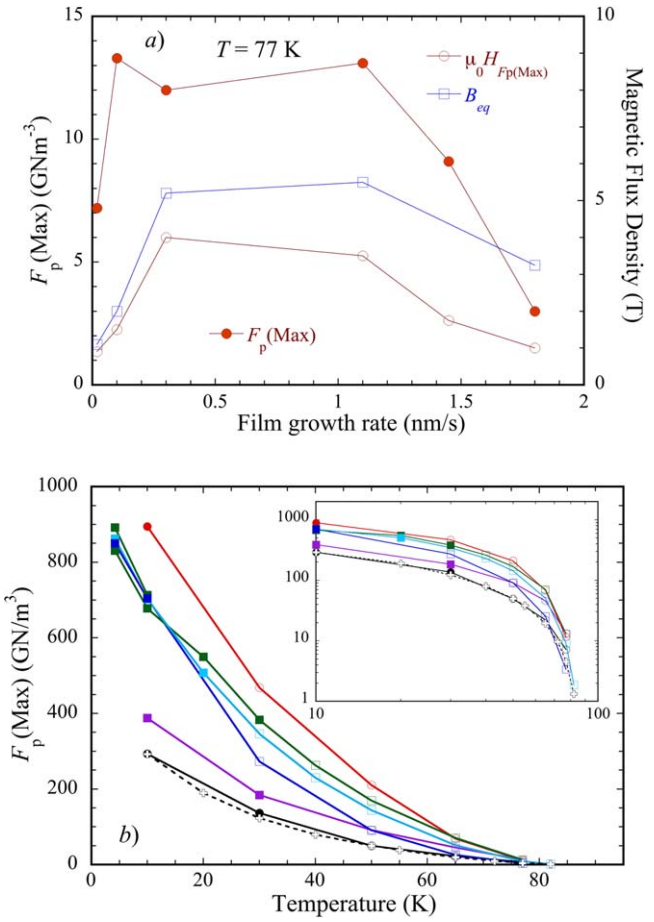

Figure 6. (a) F_p(Max) calculated from $J_c(B)$ curves at 77 K as $J_c \times \mu_0 H$ (red solid circles), magnetic field $\mu_0 H_{Fp(Max)}$ corresponds to F_p(Max) (red empty circles), and equivalent magnetic field $B_{eq} = n_{col}\,\Phi_0$ calculated from TEM analyses (blue empty squares) as a function of the film growth rate; (b) temperature dependences of the $F_{p(Max)}$ (empty symbols) for films deposited at different growth rates. At low temperatures, if the maximum of F_p was not reached, F_p values are calculated at 12 T (full symbols). The pristine YBCO sample curve is also reported for comparison (dashed line).

The corresponding F_p(Max), with $F_p = J_c \times \mu_0 H$ values, plotted in figure 6(a), increases from $\sim 4\,\mathrm{GN\,m^{-3}}$, shown by pristine YBCO films, to $7.1\,\mathrm{GN\,m^{-3}}$ for the $0.02\,\mathrm{nm\,s^{-1}}$ sample, and up to a plateau value of 12–13 $\mathrm{GN\,m^{-3}}$, shown in the rather wide *R* range from 0.1 up to $1.2\,\mathrm{nm\,s^{-1}}$. This three-fold increase with respect to the pristine YBCO confirms the effectiveness by BYNTO-related defects as strong pinning sources at 77 K. In the low *R* range and up to $R = 0.3\,\mathrm{nm\,s^{-1}}$, the position of the maximum pinning force value, $\mu_0 H_{Fp(Max)}$, shows a progressive increase and a close correspondence with B_{eq} calculated by TEM for the BYNTO column density, as can be seen very easily in figure 6(a). This is a clear confirmation that, in this *R* range, the pinning force mechanisms are dominated by the efficient interaction of vortices with a BYNTO columnar system and thus can be ultimately tuned by the film growth rate as preliminarily reported in a previous work [19]. The decrease in both F_p(Max) and $\mu_0 H_{Fp(Max)}$ values observed in the higher rate limit is consistent with the reduced vortex pinning

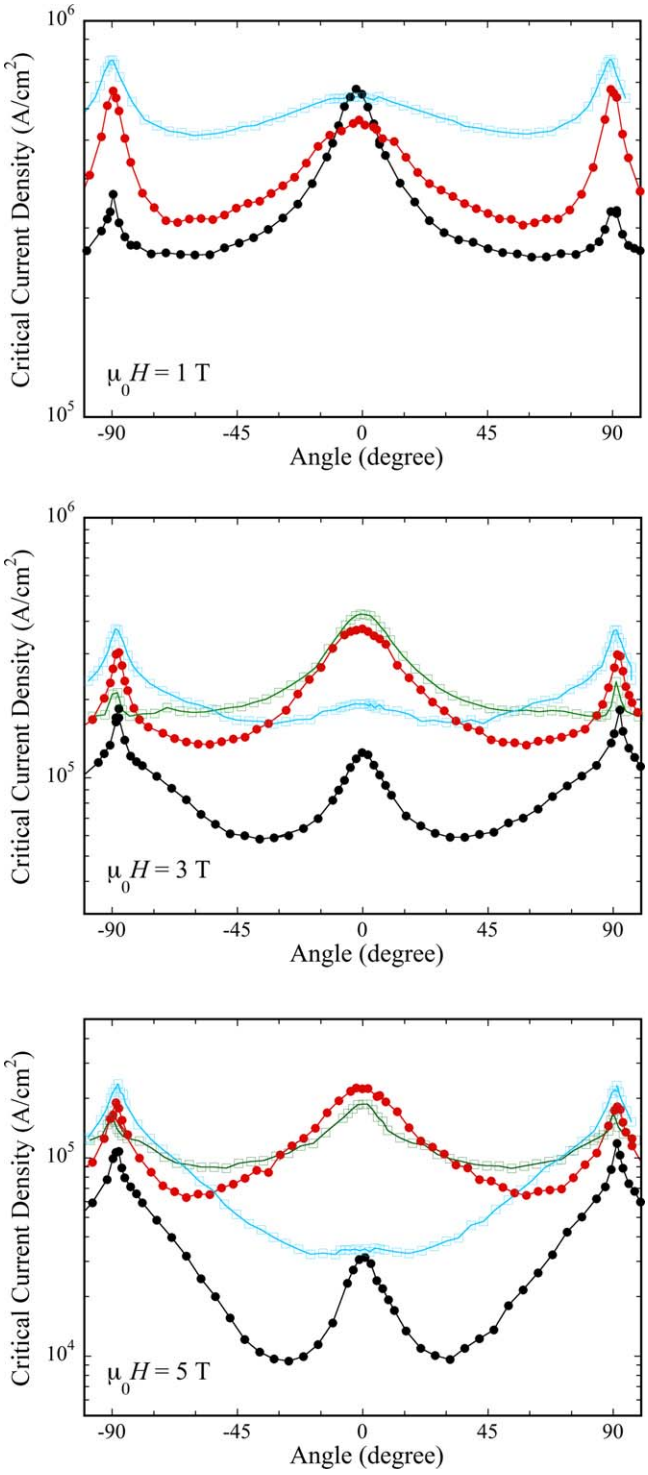

Figure 7. $J_c(\theta)$ curve dependence upon the $\mu_0 H$ direction and YBCO *c*-axis angle collected at 77 K for samples deposited with growth rates $R = 0.02\,\mathrm{nm\,s^{-1}}$ (black circles), 0.3 (red circles), 1.2 (green squares), and $1.4\,\mathrm{nm\,s^{-1}}$ (light blue squares) for $\mu_0 H = 1$ T (a), 3 T (b), and 5 T (c).

capability of the columnar system with increased splaying and the resulting loss of the matching field effect.

Angular J_c curves, shown in figure 7, are also consistent with these results. Samples deposited with $R = 0.3$ and $1.2\,\mathrm{nm\,s^{-1}}$ exhibit very intense and broad bands centred at $\theta = 0°$ ($H//c$-axis) revealing the high efficiency of the BYNTO-related defect landscape in the moderate and high field region (see figures 7(b) and (c) for 3 T and 5 T, respectively) which dominate the vortex pinning in almost the whole angular range (excluding the regions around $\theta = \pm 90°$ where *ab*-plane intrinsic pinning is active).

On the other hand, samples deposited at lower R ($=0.02\,\mathrm{nm\,s^{-1}}$ is shown in figure 7) develop sharper peaks in $J_c(\theta)$ curves, clearly discernible even for magnetic field values much greater than the equivalent field B_{eq}. The different behaviour can be attributed to the effect of the more splayed character of columnar structure already starting for samples grown at $R = 0.3$ and $1.2\,\mathrm{nm\,s^{-1}}$ with respect to $R = 0.02\,\mathrm{nm\,s^{-1}}$, as already reported in previous works on BYNTO and other APC systems [21, 44, 45]. As R is increased and the microstructure moves from columnar towards splayed nanorods, the J_c peak coherently gets weaker as observed for the sample at $R = 1.4\,\mathrm{nm\,s^{-1}}$.

These results show that, at 77 K, the mixed BYTO + BYNO doping provide a robust pinning contribution in a rather wide range of film growth rates between $R = 0.3$ and $1.2\,\mathrm{nm\,s^{-1}}$, reproducibly improving J_c in both moderate and high field regions through the occurrence of a matching field effect.

The temperature behaviour of the J_c properties can be analysed in figures 8(a) and (b) in which the $J_c(H)$ curves measured at 50 K and 10 K, respectively, are shown. As can be seen, as the temperature is reduced from 77 K, a strengthening of the J_c in-field performances of the samples deposited in the high rate limit is observed. At $T = 50$ K, the $J_c(H)$ curve recorded for sample grown at $R = 1.4\,\mathrm{nm\,s^{-1}}$ approaches the ones of samples at 0.3 and $1.2\,\mathrm{nm\,s^{-1}}$ and, at $T = 10$ K, all the YBCO-BYNTO nanocomposite films in the high rate limits, $R \geqslant 0.3\,\mathrm{nm\,s^{-1}}$, exhibit very similar performances, achieving J_c values between 7.5 and $6.0\,\mathrm{MA\,cm^{-2}}$ at 12 T. On the other hand, films deposited with lower growth rates show a worse magnetic behaviour with a larger depression in J_c in the mid- to high-field region in both temperature conditions, 50 K and 10 K. In particular, the $J_c(H)$ curves for the samples deposited at the lowest growth rate $R = 0.02\,\mathrm{nm\,s^{-1}}$ largely overlap the J_c recorded for pristine YBCO films.

Further indications on the temperature behaviour of YBCO-BYNTO samples can be obtained from F_p(Max) plotted, in figure 6(b), as a function of the temperature. As can be seen, high rate samples ($R > 0.3\,\mathrm{nm\,s^{-1}}$) exhibit a sharp increase in F_p(Max), as the temperature is reduced, resulting in higher F_p(Max) values for $T \leqslant 50$ K if compared with other samples. In the whole temperature range inspected, the optimal pinning strength is achieved for the YBCO-BYNTO film deposited with $R = 0.3\,\mathrm{nm\,s^{-1}}$, achieving about $900\,\mathrm{GN\,m^{-3}}$ at 10 K and 12 T. For this sample, an extrapolated F_p(Max) at 4.2 K in excess of $1\,\mathrm{TN\,m^{-3}}$ can be predicted, approaching the performance limits already reported for other APC systems [19, 20, 46]. On the contrary, the sample deposited at the lowest investigated growth rate value

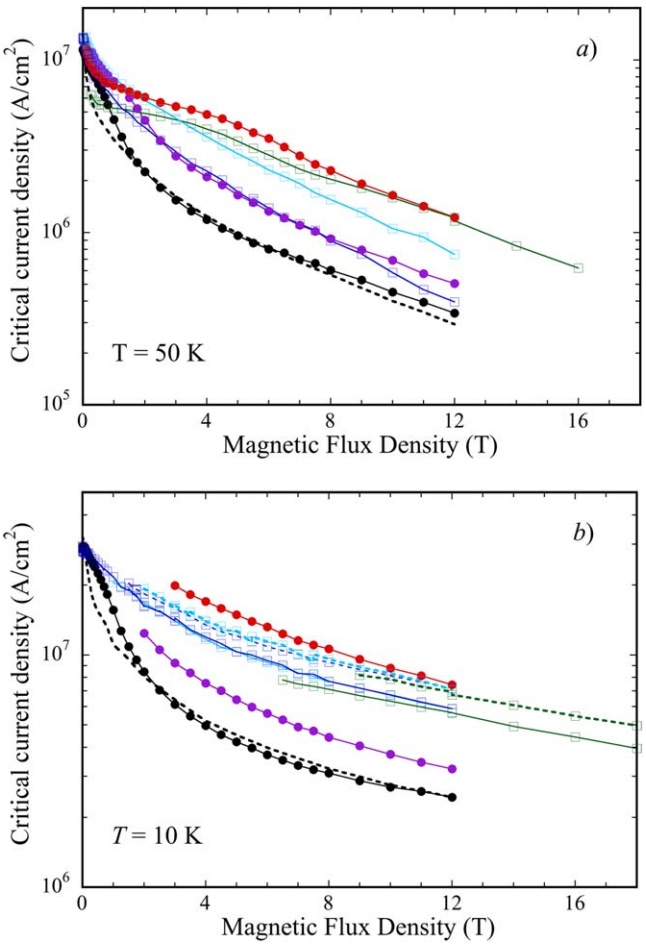

Figure 8. $J_c(H)$ curves collected at 50 K (a) and 10 K (b) for samples deposited with growth rates $R = 0.02$ nm s^{-1} (black circles), 0.1 (purple circles), 0.3 (red circles), 1.2 (green squares), 1.4 (light blue squares), and 1.8 nm s^{-1} (blue squares). Pristine YBCO sample curves are also reported for comparison (dashed lines). The dashed curves with symbols in (b) refer to the $J_c(H)$ curves measured at 4.2 K.

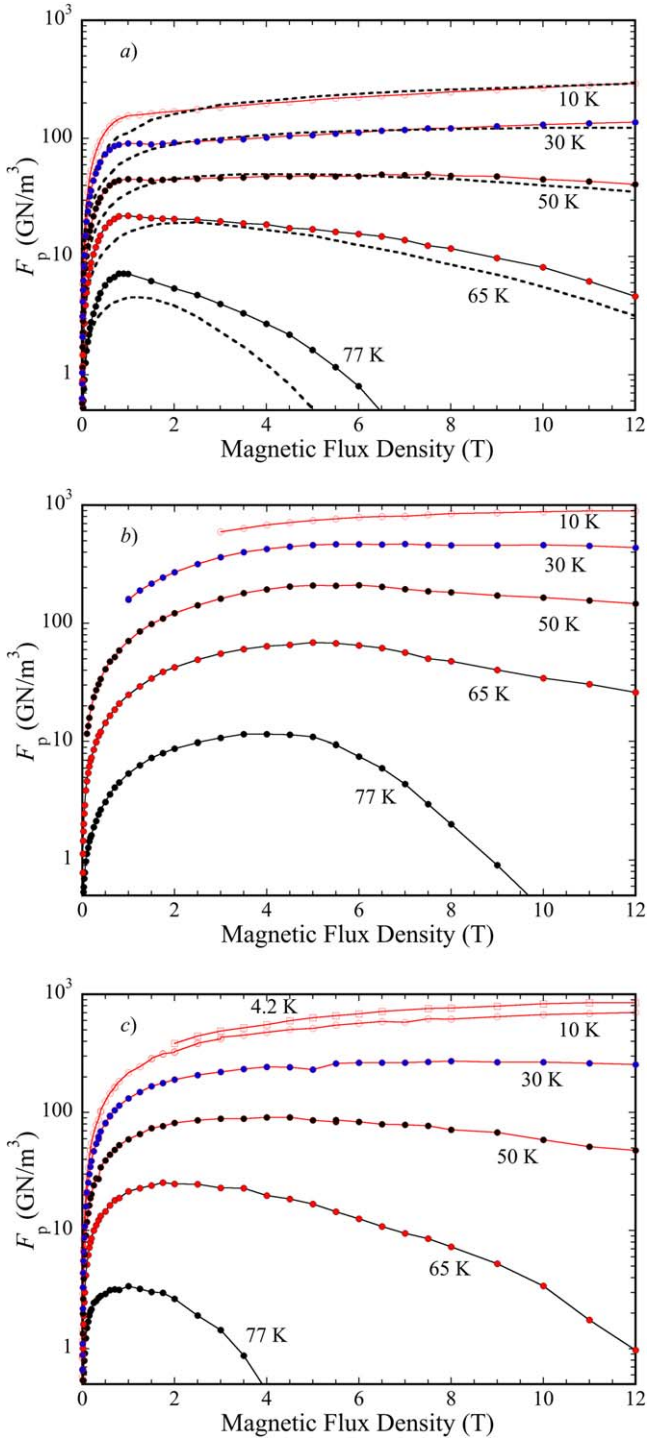

Figure 9. $F_p(H)$ curves collected at different temperatures 77 K, 65 K, 50 K, 30 K and 10 K for samples deposited with growth rates $R = 0.02$ nm s^{-1} (a), 0.3 nms^{-1} (b), and 1.8 nm s^{-1} (c). In (a), dashed lines refer to $F_p(H)$ measured on pristine YBCO film. In (c), square symbols refer to $F_p(H)$ at 4.2 K.

(0.02 nm s^{-1}) shows improved pinning performances only at 77 K, whereas for $T \leqslant 65$ K, F_p(Max) the values are very close to the ones calculated for pristine YBCO down to 10 K, further supporting the notion that, in this low rate conditions, the incorporation of BYNTO columns provides a limited benefit in the low temperature flux pinning.

The origin of this reduced effect of the temperature on the pinning efficiency can be ascribed to the dominant pinning mechanism active in these films, the matching field effect. Similar evidence of weak and limited temperature behaviour of the matching field-related improvement has been previously reported for YBCO films with 5 mol% BZO addition [33] having similar BZO n_{col}. Even in that case, the influence of APC columnar defects at low temperatures was discernible only in a low magnetic field range close to the B_{eq}. In this view, the higher F_p(Max) values at low temperatures, achieved by increasing R, can be only partly explained by the higher columnar density. In high rate YBCO-BYNTO samples, it is a different microstructure and pinning landscape which play an effective role in improving the pinning efficiency at lower temperatures.

A deeper insight can be gained with the analysis of figures 9(a)–(c), where the pinning force density $F_p(H)$ curves are plotted for selected samples deposited with $R = 0.02$, 0.3

and 1.4 nm s^{-1}. $F_p(H)$ curves for pristine YBCO films are also shown in figure 9(a), for comparison. As can be clearly recognized in figure 8(a), the low R YBCO-BYNTO film improves the F_p of the pristine sample at $T = 77$ K but, as T is reduced, the improvements in F_p are limited to the field region close to $B_{eq} = 1.1$ T. This result, together with the temperature independent maximum of F_p appearing at $\mu_0 H_{Fp(Max)} = 0.8$ T, are a direct evidence of the matching field effect. Thus, for this low growth rate sample two contributions to the vortex pinning can be identified: one related to the presence of the BYNTO columnar system, very efficient up to $\mu_0 H \approx B_{eq}$, which is superimposed to a pristine YBCO-like contribution.

The sample deposited at $R = 0.3$ nm s^{-1} shows the best F_p performance in the whole temperature and magnetic field ranges. The $F_{p(Max)}$ values are shifted to higher values approaching 5 T at lower temperatures (50 and 30 K) which is close to the estimated n_{col} for this sample ($B_{eq} \approx 5.2$ T), indicating that even for these samples the interaction of flux lines with the BYNTO columnar system dominates the pinning force (figure 9(b)). However, in this case, differently from the low rate deposited film, the pinning force contribution from BYNTO does not produce a well defined peak in a limited range of H, but leads to an effective increase of F_p in the whole magnetic field range investigated.

Finally, for the YBCO-BYNTO sample deposited at the highest growth rate $R = 1.8$ nm s^{-1}, even though the effective contribution of the BYNTO pinning centres is discernible by the remarkable improvement of transport properties, the F_p curves are more similar in shape to pristine YBCO films (figure 9(c)). This can be recognized in figures 10(a) and (b), showing that, in both pristine YBCO and 1.8 nm s^{-1} grown YBCO + BYNTO, the F_p curves can be described by the usual temperature scaling law $F_p = A(T)\, f_p(h)$, with f_p a function of the reduced magnetic field $h = H/H_{Fp(Max)}$, $f_p(h) = h^{\beta}\,(1\text{-}h)^{\gamma}$ [47, 48]. The scalability of the F_p curves implies that a single mechanism of vortex pinning is active in the invesigated temperature range. The same features are recognized for the sample deposited at $R = 1.4$ nm s^{-1}. On the contrary, for samples grown with $R \leqslant 1.2$ nm s^{-1}, the F_p scaling law cannot be applied due to the presence of two pinning contributions with comparable strength with different temperature dependences, as shown in figure 10(c). Therefore, the introduction of the mixed BYNO + BYTO secondary phases generates different vortex pinning effective defect landscapes depending on the growth rates: at low rates a strong correlated pinning related to the columnar system is superimposed on an isotropic mechanism; at high growth rates, the mechanism cannot be identifiable with BYNTO columns or c-axis correlated nanorods but with a more complex scenario related to the presence of BYNTO. The peculiar feature of this complex pinning landscape is its strong effectiveness at low temperatures.

This is fully consistent with what has been observed by TEM investigations: by increasing R, BYNTO defects change from sparse and relatively large columns to denser and thinner columns with increased density of decorating Y_2O_3 nanoparticles. By further increaing R increase, the BYNTO columns start to form nanorods and meandered columns with extremely low size down to 3 nm, as well as an increased number of stacking faults. It is likely that these two defect landscapes are present in the optimal YBCO-BYNTO nanocomposite film deposited at $R = 0.3$ nm s^{-1}, leading to superior performances of that sample over the whole temperature and magnetic field ranges.

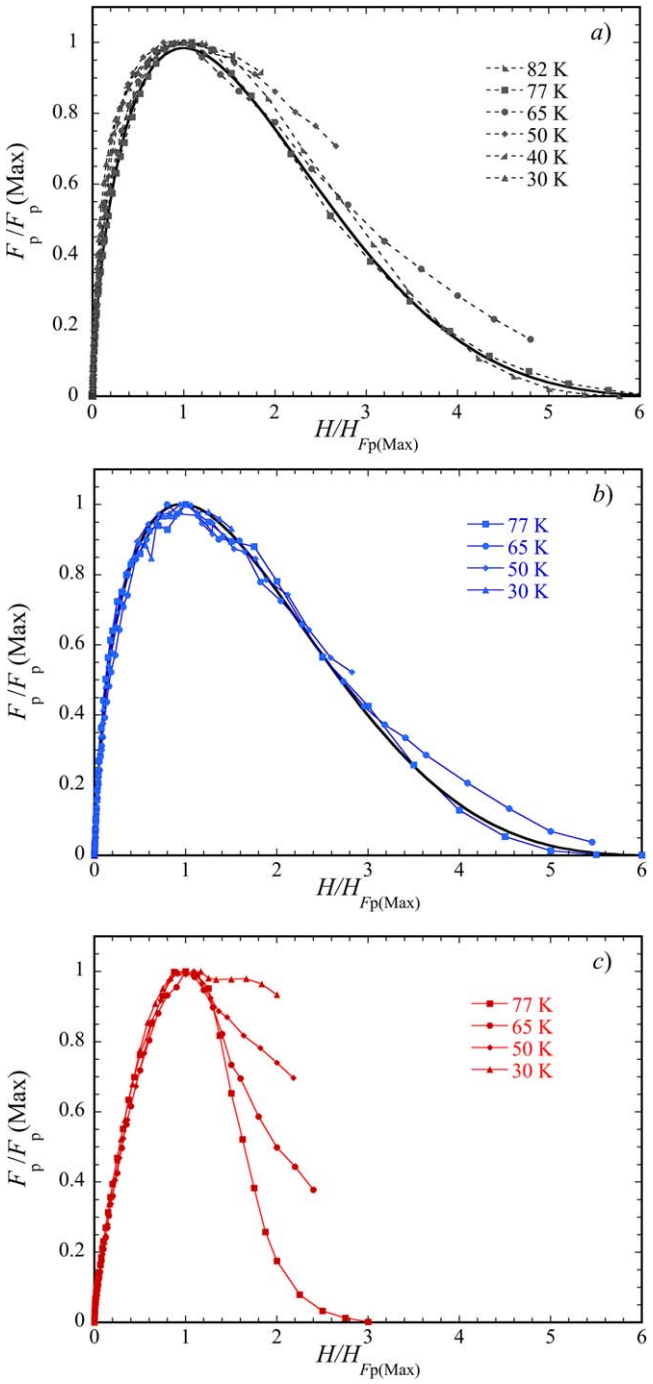

Figure 10. Scaling law for $F_p(H)/F_p(\text{Max})$ curves collected at different temperatures for pristine YBCO film (a), YBCO-BYNTO film deposited with growth rates $R = 1.8$ nm s^{-1} (b), and 0.3 nm s^{-1} (c). Continuous black lines are the fits with $f_p(h) = h^{\beta}\,(1\text{-}h)^{\gamma}$. Best fits are obtained with $\beta = 0.66$ (a), 0.61 (b) and $\gamma = 4$ (a), 3.5 (b). The scaling law in (c) cannot be applied.

4. Conclusions

In this work, over the whole temperature range down to 4.2 K, the influence of the film growth rate, R, on the structural and J_c properties of YBCO epitaxial films with incorporated 2.5 mol% BYTO and 2.5 mol% BYNO double perovskite secondary phases has been investigated. It is found that the nanocomposite microstructure is strongly affected by the variation in the film growth rate within the range $R = 0.02$–$1.8\ \mathrm{nm\ s^{-1}}$. In particular, from TEM analyses, it was observed that in the low R limit the microstructure is characterized by a straight BYNTO columnar structure that switches to meandered and truncated nanorods in the opposite high rate limit, with the crossover value being between $R \approx 0.3$–$1.2\ \mathrm{nm\ s^{-1}}$. The different nature of the BYNTO segregation is observed by XRD measurements which reveal a change in the shape and shift in the angle position reflection peak. A possible explanation for this feature of a reduction of strain at the BYNTO/YBCO interface, through Y loss into the BYNTO lattice ($Ba_2Y_x(Nb,Ta)_{2-x}O_6$ $(0 \leqslant x \leqslant 1)$) is proposed. The BYNTO columnar microstructure results in very efficient flux pinning at 77 K providing the chance of tuning the extension of the plateau in the $J_c(H)$ curves and, correspondingly, the maximum in the $F_p(H)$ by varying the film growth rate up to $0.3\ \mathrm{nm\ s^{-1}}$. An F_p as high as $13.5\ \mathrm{GN\ m^{-3}}$ and an irreversibility field in excess of 11 T is obtained in these films. The film deposited at a middle rate, $R = 0.3\ \mathrm{nm\ s^{-1}}$, exhibits the best performances over the whole temperature and magnetic field range, achieving the maximum $F_p = 900\ \mathrm{GN\ m^{-3}}$ at 10 K and 12 T. From the analysis of the $F_p(H, T)$ curves, it is shown that in YBCO-BYNTO films deposited in the high R limit a different vortex pinning is set up which is not dominated by BYNTO columnar defects. Here, a microstructure characterized by BYNTO nanorods and meandered columns, together with short stacking faults, is generated which, even though it produces a limited improvement in J_c properties at 77 K, exhibits a strong J_c improvement at lower temperature with F_p values of $700\ \mathrm{GN\ m^{-3}}$ at 10 K, 12 T and $900\ \mathrm{GN\ m^{-3}}$ at 4.2 K, 18 T. This is a promising result in view of the development of REBCO-based coated conductors for applications requiring high field conditions, such as large magnets for nuclear fusion reactors and particles accelerators. Finally, as a general remark, this study points out that the complex defects landscape developed in nanocomposite YBCO with APCs requires complete temperature characterization of the J_c behaviour to understand the subtleties of the different operative pinning mechanisms in the obtained complex pinning landscape.

Acknowledgments

This work was partially financially supported by EUROTAPES, a collaborative project funded by the European Commission's Seventh Framework Program (FP7/2007–2013) under Grant Agreement No. 280432. This work has been partially carried out within the framework of the EUROfusion Consortium and has received funding from the Euratom programme 2014–2018 and 2019–2020 under Grant Agreement No. 633053. The views and opinions expressed herein do not necessarily reflect those of the European Commission.

This project has received funding from the European Union's Horizon 2020 research and innovation programme under Grant Agreement No. 823717—ESTEEM3 (Nano-engineered YBCO superconducting tapes for high field applications, NESTApp). GC acknowledges the support of Michele De Angelis for XRD measurements and calculations.

ORCID iDs

G Celentano https://orcid.org/0000-0001-6017-0739
F Rizzo https://orcid.org/0000-0002-7710-5084
A Augieri https://orcid.org/0000-0002-0942-0752
A Mancini https://orcid.org/0000-0002-4148-1010
A Vannozzi https://orcid.org/0000-0003-4628-4312
J L MacManus-Driscoll https://orcid.org/0000-0003-4987-6620
J Feighan https://orcid.org/0000-0002-5222-7034
A Meledin https://orcid.org/0000-0002-3200-0553
J Mayer https://orcid.org/0000-0003-3292-5342

References

[1] Crisan A, Fujiwara S, Nie J C, Sundaresan A and Ihara H 2001 *Appl. Phys. Lett.* **79** 4547–9
[2] McManus-Driscoll J L *et al* 2004 *Appl. Phys. Lett.* **84** 5329–31
[3] MacManus-Driscoll J L, Foltyn S R, Jia Q X, Wang H, Serquis A, Civale L, Maiorov B, Hawley M E, Maley M P and Peterson D E 2004 *Nat. Mater.* **3** 439
[4] Gutiérrez J *et al* 2007 *Nat. Mater.* **6** 367
[5] Huang J, Tsai C-F, Chen L, Jian J, Khatkhatay F, Yu K and Wang H 2014 *J. Appl. Phys.* **115** 123902
[6] Haugan T, Barnes P N, Wheeler R, Meisenkothen F and Sumption M 2004 *Nature* **430** 867–70
[7] Goyal A *et al* 2005 *Supercond. Sci. Technol.* **18** 1533–8
[8] Tobita H, Notoh K, Higashikawa K, Inoue M, Kiss T, Kato T *et al* 2012 *Supercond. Sci. Technol.* **25** 062002
[9] Mele P *et al* 2008 *Supercond. Sci. Technol.* **21** 032002
[10] Chen Y, Selvamanickam V, Zhang Y, Zuev Y L, Cantoni C, Specht E D, Paranthaman M, Aytug T, Goyal A and Lee D F 2009 *Appl. Phys. Lett.* **94** 062513–5
[11] Foltyn S R, Civale L, MacManus-Driscoll J L, Jia Q X, Maiorov B, Wand H and Maley M 2007 *Nat. Mater.* **6** 631–42
[12] Feighan J, Kursumovic A and MacManus-Driscoll J L 2017 *Supercond. Sci. Technol.* **30** 123001
[13] links for most of the HTS coated conductors suppliers can be found in https://superconductorweek.com/industry-directory/industry-links/
[14] Fietz W *et al* 2013 *Fus. Eng. Design* **88** 440–5
[15] Bruzzone P *et al* 2015 *Fus. Eng. Design* **96-97** 77–82
[16] Bottura L, de Rijk G, Rossi L and Todesco E 2012 *IEEE Trans. Appl. Supercond.* **22** 4002008
[17] Usoskin A *et al* 2018 *IEEE Trans. Appl. Supercond.* **28** 6602506

[18] Xu A, Delgado L, Khatri N, Liu Y, Selvamanickam V, Abraimov D, Jaroszynski J, Kametani F and Larbalestier D C 2014 *APL Mater.* **2** 046111
[19] Miura S, Tsuchiya Y, Yoshida Y, Ichino Y, Awaji S, Matsumoto K, Ibi A and Izumi T 2017 *Supercond. Sci. Technol.* **30** 084009
[20] Majkic G, Pratap R, Xu A, Galstyan E, Higley H C, Prestemon S O, Wang X, Abraimov D, Jaroszynski J and Selvamanickam V 2018 *Supercond. Sci. Technol.* **31** 10LT01
[21] Rizzo F *et al* 2018 *Nanoscale* **10** 8186
[22] Galstyan E, Pratap R, Majkic G, Kochat M, Mohan V and Selvamanickam V 2019 *IEEE Trans. Appl. Supercond.* **29** 8001206
[23] Li Z, Coll M, Mundet B, Chamorro N, Vallès F, Palau A, Gazquez J, Ricart S, Puig T and Obradors X 2019 *Sci. Rep.* **9** 5828
[24] Cantoni C, Gao Y, Wee S H, Specht E D, Gazquez J, Meng J, Pennycook S J and Goyal A 2011 *ACS Nano* **5** 4783–9
[25] Llordes A *et al* 2012 *Nat. Mater.* **11** 329
[26] Holesinger T G *et al* 2008 *Adv. Mater.* **20** 391–407
[27] Augieri A *et al* 2018 *IEEE Trans. Appl. Supercond.* **28** 7500604
[28] Ercolano G, Harrington S A, Wang H, Tsai C F and MacManus-Driscoll J L 2010 *Supercond. Sci. Technol.* **23** 022003
[29] Opherden L *et al* 2016 *Sci. Rep.* **6** 21188
[30] Rizzo F *et al* 2016 *APL Mater* **4** 061101
[31] Pahlke P *et al* 2018 *Supercond. Sci. Technol.* **31** 044007
[32] Singh R K and Kumar D 1998 *Mater. Sci. Eng. Rep.* **22** 113–85
[33] Augieri A *et al* 2010 *J. Appl. Phys.* **108** 063906
[34] Nelson J B and Riley D P 1945 *Proc. Phys. Soc.* **57** 160–77
[35] Kovács A, Schierholz R and Tillmann K 2016 *J. Large-scale Res. Facil.* **2** A43
[36] Horide T, Kametani F, Yoshioka S, Kitamura T and Matsumoto K 2017 *ACS Nano* **11** 1780–8
[37] Piperno L *et al* 2019 *Appl. Surf. Sci.* **484** 237–44
[38] Feldmann D M, Holesinger T G, Maiorov B, Foltyn S R, Coulter J Y and Apodaca I 2011 *Supercond. Sci. Technol.* **23** 095004
[39] Wu J and Shi J 2017 *Supercond. Sci. Technol.* **30** 103002
[40] Miura S, Yoshida Y, Ichino Y, Xu Q, Matsumoto K, Ichinose A and Awaji S 2016 *APLMater* **4** 016102
[41] Selinder T I, Helmersson U, Han Z and Wallenberg L R 1993 *Thin Solid Films* **229** 237–48
[42] Reich E, Thersleff T, Huhne R, Iida K, Schultz L and Holzapfel B 2009 *Supercond. Sci. Technol.* **22** 105004
[43] structural properties can be found in https://materialsproject.org/ (Materials Project web-based database) and http://crystallography.net/cod/ (Crystallography Open Database)
[44] Ercolano G, Bianchetti M, Sahonta S L, Kursumovic A, Lee J H, Wang H and MacManus-Driscoll J L 2014 *J. Appl. Phys.* **116** 033915
[45] Maiorov B, Baily S A, Zhou H, Ugurlu O, Kennison J A, Dowden P C, Holesinger T G, Foltyn S R and Civale L 2009 *Nat. Mater.* **8** 398
[46] Goyal A and Wee S H 2017 *J. Phys.: Conf. Ser.* **871** 012039
[47] Fietz W A and Webb W W 1969 *Phys. Rev.* **178** 657–67
[48] Kramer E J 1973 *J. Appl. Phys.* **44** 1360–70